JOURNAL OF SPACECRAFT AND ROCKETS
Vol. 31, No. 5, September–October 1994

Application of the Multigrid Solution Technique to Hypersonic Entry Vehicles

Francis A. Greene*
NASA Langley Research Center, Hampton, Virginia 23681

Multigrid techniques have been incorporated into an existing hypersonic flow analysis code, the Langley aerothermodynamic upwind relaxation algorithm. The multigrid scheme is based on the full approximation storage approach and uses full multigrid to obtain a well-defined fine-mesh starting solution. Predictions were obtained using standard transfer operators, and a V cycle was used to control grid sequencing. Computed hypersonic flow solutions, compared with experimental data for a 15-deg blunted sphere-cone and a blended-wing body, are presented. It is shown that the algorithm predicts heating rates accurately, and computes solutions in one-third the computational time of the nonmultigrid algorithm.

Nomenclature

$\mathbf{A}$	= Jacobian matrix of $\boldsymbol{g}$ with respect to $\boldsymbol{q}$
AR	= cell aspect ratio
a	= sound speed, m/s
$\mathbf{B}$	= Jacobian matrix of $\boldsymbol{h}$ with respect to $\boldsymbol{q}$
$\boldsymbol{g}$	= inviscid flux vector
$\boldsymbol{h}$	= viscous flux vector
$\mathbf{I}$	= identity matrix
kemsh	= current mesh level
$\mathbf{L}$	= axial reference length, m
$\mathbf{M}$	= right eigenvector matrix of $\mathbf{A}$
$\mathbf{M}^{-1}$	= left eigenvector matrix of $\mathbf{A}$
memsh	= current fine-mesh level
n	= iteration counter
$\boldsymbol{n}$	= outward unit normal vector of a cell face
nmesh	= finest-mesh level
$\mathbf{Q}$	= heating rate, W/m^2
RN	= cone nose radius, m
r_I	= inviscid relaxation factor
r_V	= viscous relaxation factor
$\mathbf{S}$	= circumferential arclength distanc e, m
t	= time, s
U, V, W	= contravariant velocities on a cell face, m/s
$\mathbf{X}$	= axial distance, m
$\mathbf{Y}$	= spanwise distance, m
κ	= aspect-ratio scale factor
λ	= eigenvalue matrix of $\mathbf{A}$
σ	= cell face area, m^2
Ω	= cell volume, m^3

Introduction

DURING the last decade, the performance of supercomputers and the realm of applications for computational fluid dynamic (CFD) algorithms have increased several fold. Increases in memory, and advances in hardware and processor speed, combined with the continued improvement of numerical algorithms and surface and volume grid generation techniques, have made obtaining computational solutions for complex three-dimensional geometries a reality.[1–5] However, in spite of the advances, these computations are far from routine and are computationally feasible only when the grid size is considered a priori. With grid size driving computer memory and CPU time, tradeoffs are typically employed to arrive at a minimum grid size that will give accurate results in the region of interest, forsaking other regions. The solution of the Navier-Stokes equations for a nonequilibrium flow over a realistic geometry using a grid with sufficient resolution to properly interpret all hypersonic flow phenomena requires hundreds of hours of Cray-2 time. It is estimated that a solution of this type over the Shuttle Orbiter will require up to 0.5 gigawords of memory and 500 Cray-2 hours.[5] If solutions over configurations of this size are to become routine, algorithm memory and CPU time requirements need to be reduced. The memory issue has been addressed by Weilmuenster and Gnoffo.[5] The present work concentrates on the time part of the equation through the use of the multigrid solution technique.[6]

The convergence of most single-grid algorithms is rapid at the start. This initial rapid convergence is associated with the removal of high-frequency errors from the solution. Most relaxation schemes handle this aspect satisfactorily, but some better than others. Convergence deteriorates when low-frequency errors are present. It is in attempting to remove these low-frequency errors that the majority of the computational time is expended. Multigrid involves passing information from a fine mesh to successively coarser meshes, where corrections to the finer-mesh solution are computed and transferred back to the fine mesh. In the context of multigrid, fine meshes are used to remove high-frequency errors, whereas coarse meshes are used to remove low-frequency errors. Low-frequency errors on a fine mesh, when transferred to a coarse mesh, resemble high-frequency errors. If the algorithm dampens high-frequency errors efficiently, the relaxation of the solution on the coarse mesh quickly dampens what were fine-mesh low-frequency errors. This process speeds convergence by removing high- and low-frequency errors at similar rates. Crucial to the success of multigrid is a numerical algorithm that efficiently dampens high-frequency errors.

The multigrid technique has been used with great success on the Euler and Navier-Stokes equations for subsonic and transonic flow.[7–9] Although initially applied to problems containing small regions of supersonic flow, multigrid has recently been successfully applied to viscous perfect-gas flows that are supersonic or faster outside the boundary layer.[10–13] The work in Refs. 10–13 demonstrated the modifications needed to overcome the interactions of multigrid with strong shocks. While most of the solutions were two-dimensional or low-angle-of-attack three-dimensional solutions, Vatsa[14] has computed the Mach 6 flow over a shuttle-like geometry at a high angle of attack and obtained a significant speedup over with nonmultigrid algorithms.

In light of these successes, multigrid techniques have been incorporated in the Langley aerothermodynamic upwind relaxation algorithm (LAURA). The LAURA computer program, as initially developed by Gnoffo,[15] was a three-dimensional finite-volume thin-layer Navier-Stokes solver for computing perfect-gas blunt-body and wake flows. Gnoffo has subsequently extended LAURA to

Received June 9, 1993; revision received Feb. 15, 1994; accepted for publication Feb. 17, 1994.

*Aerospace Engineer, Aerothermodynamics Branch, Space Systems Division. Senior Member AIAA.

compute flows in thermal and chemical nonequilibrium.[16] The LAURA algorithm has been validated against computational and/or experimental heat-transfer data on slender, blunt, and winged vehicles.[2–4,17] The code has been used extensively in support of agency activities connected with the Shuttle Orbiter experiments and Aeroassisted Flight Experiment (AFE) programs. The successful application of the LAURA code to several vehicle classifications, and its use over a wide hypersonic Mach-number range, demonstrates the robust nature of the algorithm.

This work is not intended to be a multigrid CFD study. Rather, the sole intention was to reduce the CPU time the LAURA algorithm requires to compute a solution. This has significance for problems that demand large amounts (on the order of hours) of CPU time, since a small reduction in CPU time can provide a meaningful saving of computer resources. To have an effect on parametric studies, the time per solution for the code will have to be reduced by at least a factor of two. The object of the work reported herein is to determine if multigrid techniques can aid in achieving this time reduction. Admittedly, the solution procedure used in LAURA is not the best suited, in terms of high-frequency damping, for multigrid applications, but it is very robust for geometrically complex vehicles at high hypersonic conditions. For this reason, it was decided that at this point the solution procedure would not be changed to achieve better high-frequency damping. While the method for solving the governing equations was unaltered, modifications to the left-hand side of the governing equations were made that enhance the damping characteristics and enable improved convergence. For this study, heat-transfer predictions for the Mach 10.6 flow over a 15-deg blunted sphere-cone at 20-deg angle of attack and for the Mach 16.7 flow over a blended-wing body (BWB) configuration at 6-deg angle of attack are presented. LAURA predictions from the multigrid code are compared with experimental data.[18,19] All predictions assume laminar perfect-gas flow.

Governing Equations

A multigrid solution procedure was incorporated in the LAURA algorithm described in Ref. 20. The following paragraphs give a summary of the formulation of the governing equations.

Following the form given in Ref. 15, the integral form of the governing equations is expressed

$$\int\int\int \mathbf{q}_t \, d\Omega + \int\int (\boldsymbol{f}\cdot\boldsymbol{n})\, d\sigma = 0 \tag{1}$$

where $\mathbf{q}_t$ represents the time rate of change of the dependent variable vector $\mathbf{q}$, and $\boldsymbol{f}$ represents the sum of the inviscid and viscous flux. Expressing Eq. (1) in finite-volume form for a single six-sided cell in the computational domain gives

$$\begin{aligned}\delta\mathbf{q}_{i,j,k} = &-\left[\frac{\delta t}{\Omega}\right]_{i,j,k}\left[\boldsymbol{f}_{i+\frac{1}{2}}\cdot\boldsymbol{n}_{i+\frac{1}{2}}\sigma_{i+\frac{1}{2}} - \boldsymbol{f}_{i-\frac{1}{2}}\cdot\boldsymbol{n}_{i-\frac{1}{2}}\sigma_{i-\frac{1}{2}}\right]_{j,k}\\ &+\left[\boldsymbol{f}_{j+\frac{1}{2}}\cdot\boldsymbol{n}_{j+\frac{1}{2}}\sigma_{j+\frac{1}{2}} - \boldsymbol{f}_{j-\frac{1}{2}}\cdot\boldsymbol{n}_{j-\frac{1}{2}}\sigma_{j-\frac{1}{2}}\right]_{i,k}\\ &+\left[\boldsymbol{f}_{k+\frac{1}{2}}\cdot\boldsymbol{n}_{k+\frac{1}{2}}\sigma_{k+\frac{1}{2}} - \boldsymbol{f}_{k-\frac{1}{2}}\cdot\boldsymbol{n}_{k-\frac{1}{2}}\sigma_{k-\frac{1}{2}}\right]_{i,j}\end{aligned} \tag{2}$$

where δ represents the time change in the quantity to its right. The lowercase subscripts indicate values at cell center, unless offset by a half, in which case they indicate values at the center of a cell face. A shorthand notation that will be used in this paper enables Eq. (2) to be written as

$$\delta\mathbf{q}_{i,j,k} = \left[\frac{\delta t}{\Omega}\right]_{i,j,k}\sum_{l=i,j,k}\left\{[(\boldsymbol{g}+\boldsymbol{h})\cdot\boldsymbol{n}\sigma]_{l-\frac{1}{2}} - [(\boldsymbol{g}+\boldsymbol{h})\cdot\boldsymbol{n}\sigma]_{l+\frac{1}{2}}\right\}$$

where $\boldsymbol{g}$ and $\boldsymbol{h}$ are the inviscid and viscous portions of $\boldsymbol{f}$, respectively.

The first-order inviscid flux at the center of a cell face is computed using Roe's scheme,[21] and second-order fluxes are computed using Yee's symmetric total-variation-diminishing (STVD) approach.[22] The inviscid flux is defined as

$$\boldsymbol{g}_{l+\frac{1}{2}} = \tfrac{1}{2}\left\{\boldsymbol{g}(\boldsymbol{q}_l) + \boldsymbol{g}(\mathbf{q}_{l+1}) - [\mathbf{M}|\lambda|(\mathbf{d}-\mathbf{d}^{\min})]_{l+\frac{1}{2}}\right\}$$

where

$$\mathbf{d}_{l+\frac{1}{2}} = \mathbf{M}^{-1}_{l+\frac{1}{2}}\Delta\mathbf{q}_{l+\frac{1}{2}} \tag{3}$$

and

$$\mathbf{d}^{\min} = \min\ \mathrm{mod}[\mathbf{d}_1, \mathbf{d}_2, \mathbf{d}_3]$$

The subscripts 2, 1, and 3 refer to the face at which the flux is being computed, the face behind, and the face ahead, respectively. The Δ represents the spatial change in the quantity to its right. The right ($\mathbf{M}$) and left ($\mathbf{M}^{-1}$) eigenvector matrices and the eigenvalue λ matrix are given in Ref. 15. Second-order central differences are used to approximate the viscous stress and heat flux.

Because Roe's method permits nonphysical solutions in the vicinity of near-zero eigenvalues, the elements of λ are limited as shown below:

$$\lambda = \begin{cases} |\lambda| & \text{if } |\lambda| \geq 2\varepsilon \\ \lambda^2/4\varepsilon + \varepsilon & \text{if } |\lambda| < 2\varepsilon \end{cases}$$

where

$$\varepsilon = \varepsilon_0(a + |U| + |V| + |W|), \qquad 0.1 \leq \varepsilon_0 \leq 0.3$$

is used in the directions tangent to the body, and

$$\varepsilon = \kappa\varepsilon_0(a + |U| + |V| + |W|), \qquad 0.1 \leq \varepsilon_0 \leq 0.3$$

is used in the direction normal. The value κ is based on the cell aspect ratio (AR) and follows the form given in Ref. 5 as

$$\kappa = \min(1, \widetilde{\mathrm{AR}})$$

For the multigrid technique to begin on the coarsest mesh, if was necessary to modify AR. The aspect ratio is set to 1 on the coarsest mesh (kmesh = 1) and is scaled on successively finer meshes, until it takes on its unmodified value on the finest mesh (kmesh = nmesh).

$$\widetilde{\mathrm{AR}} = 1 - \frac{(1-\mathrm{AR})(\mathrm{kmesh}-1)}{\mathrm{nmesh}-1}$$

Accounting for both inviscid and viscous terms, the implicit form of the governing equations is

$$\left[\mathbf{I} + \frac{\delta t}{\Omega}\mathbf{C}\right]^n_{i,j,k}\delta\mathbf{q}^n_{i,j,k} = \mathbf{r}^n_{i,j,k} + \tau_{i,j,k} = \mathbf{R}_{i,j,k} \tag{4}$$

where

$$\mathbf{C}_{i,j,k} = \sum_{l=i,j,k}\left[\left(\frac{r_I}{2}|\mathbf{A}| + r_V\mathbf{B}\right)\sigma_{l+\frac{1}{2}} + \left(\frac{r_I}{2}|\mathbf{A}| + r_V\mathbf{B}\right)\sigma_{l-\frac{1}{2}}\right]$$

and

$$\mathbf{r}^n_{i,j,k} = \left[\frac{\delta t}{\Omega}\right]_{i,j,k}\sum_{l=i,j,k}\left\{[(\boldsymbol{g}+\boldsymbol{h})\cdot\boldsymbol{n}\sigma]_{l-\frac{1}{2}} - [(\boldsymbol{g}+\boldsymbol{h})\cdot\boldsymbol{n}\sigma]_{l+\frac{1}{2}}\right\}$$

Here τ is a forcing function and results from incorporating the multigrid solution procedure. Details concerning its value are contained in the Multigrid section. Information on boundary and initial conditions can be found in Ref. 15. Boundary values for the fine and coarse mesh problems are updated every iteration. For first-order solutions, the inviscid and viscous relaxation factors (r_I, r_V) associated with the Jacobian matrices are 1.5 and 1.0, respectively. The inviscid relaxation factor for a second-order solution is increased as a function of work from 1.5 to a maximum of 2.3. Similarly, the second-order viscous factor ranges from 0.7 to 1.0. After converging a second-order solution and prior to moving to a finer mesh, the second-order inviscid and viscous relaxation factors are reset to 1.5 and 0.7, respectively. Empirical evidence indicates that increasing the relaxation factors prevents the convergence of the solution from stalling by damping perturbations occurring at the shock.

Multigrid

The full approximation storage (FAS) scheme proposed by Brandt[6] is incorporated in the LAURA algorithm. Full multigrid (FMG) is used to obtain a well-defined starting solution for the fine-mesh problem, and a standard V cycle is used to control grid sequencing. Coarser-level grids are created using full coarsening, in which every other grid line in each coordinate direction is removed. Fluxes are second-order accurate only when on the fine grid, and only when this level is the finest (nmesh) or one below (nmesh − 1). At all other levels, the fluxes are first-order accurate. The use of second-order fluxes on level nmesh − 1 was found to speed convergence, by providing an improved starting point for the solution on the finest grid. For both the fine- and the coarse-mesh problem, the viscous terms are included. A single multigrid cycle consists of four relaxation sweeps on the coarser meshes and two sweeps on the fine mesh. The need for multiple fine-mesh iterations per cycle can be attributed to poor high-frequency damping inherent in the solution algorithm. The governing equations are solved with a constant Courant number on the order of 10.

The forms of the governing equations for the nonmultigrid and multigrid algorithms differ only by the term τ. The forcing function τ is a measure of the relative truncation error and insures that the coarse-mesh solution is driven by the fine-mesh residual. For computations performed on the fine mesh, τ is zero. For a coarse mesh, τ is defined as

$$\tau = [\mathbf{R} - \mathbf{r}(\mathbf{q}^{n=1})]$$

where $\mathbf{R}$ is the residual restricted from the next finer mesh, and $\mathbf{r}(\mathbf{q}^{n=1})$ is computed based on restricted $\mathbf{q}$ values.

A volume-weighted restriction operator is used to transfer the solution and residual to coarser meshes. Corrections to solutions are moved to the finer mesh (prolonged) with trilinear interpolation. On highly stretched meshes, this prolongation operator can add high-frequency errors to the corrections. As noted in Ref. 10, to dampen some of this added noise, the corrections are smoothed using a constant-coefficient Laplacian-type smoother before being added to the fine-mesh solution. The coefficient used in this work was 0.3.

Experimental Data and Models

Sphere-Cone

Cleary's[18] experimental heat-transfer data for a 15-deg sphere-cone have been used in the past for comparisons with computational techniques. In this experiment, tests were performed to determine the effects of angle of attack and nose bluntness on laminar heating rates. The cone nose radius varied from 0 to 0.028 m, and the angle of attack ranged from 0 to 20 deg. Well-instrumented sphere-cones were exposed to a Mach 10.6 flow with a Reynolds number of 4.7×10^6 m^{-1}. Heat-transfer gauges were distributed from the leeside to the windside in 15-deg increments at ten streamwise stations. A cone at 20-deg angle of attack with a 0.028-m nose radius was selected for comparison. While a sphere-cone is not a complex geometry, at 20-deg angle of attack it displays some of the same three-dimensional flow phenomena associated with more complex geometries. In this case, the ability of the code to handle separated flow is explored.

Blended Wing-Body

More typical of geometries associated with National Aerospace Plane (NASP) applications is the blended wing-body (BWB) shown in Fig. 1. This is the configuration upon which heat-transfer measurements were taken in the Calspan shock tunnel.[19] Designed for code calibration, the model was instrumented at over 100 locations. Heating-rate measurements were obtained for varying Mach and Reynolds numbers at 0-, 6- and 10-deg angles of attack. These experiments provided information around the vehicle's circumference at several axial locations, and along the upper and lower symmetry planes.

As shown in Fig. 1, the rounded upper surface blends to a sharp leading edge, and two compression ramps are on the lower surface. The computational model was created by truncating a numerical representation of the experimental geometry just forward of the fins. The two models are identical forward of the fins. Heat-transfer predictions were made at Mach 16.7 for a Reynolds number of 4.2×10^5 m^{-1}. Data distributed along the upper and lower symmetry planes, as well as in the circumferential direction at four streamwise stations, for a flow at 6-deg angle of attack are presented for comparison.

Table 1 Freestream conditions

Case	Geometry	T_∞, K	M_∞	α, deg	Re, m^{-1}
I	Cone	47.3	10.6	20	4.7×10^6
II	BWB	46.6	16.7	6	4.2×10^5

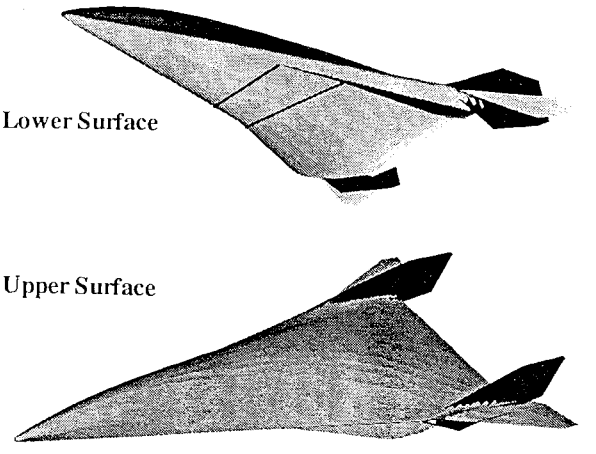

Fig. 1 The blended wing-body geometry.

Results and Discussion

Surface heating-rate predictions from LAURA are compared with experimental data. The freestream conditions for the cases presented are listed in Table 1. All computed predictions were performed on a CrayY-MP.

Sphere-Cone

Heating-rate predictions from LAURA were compared with the experimental data from Ref. 18. A Mach 10.6 flow with a freestream Reynolds number equal to 4.7×10^6 m^{-1} was selected as the test condition. The angle of attack was 20 deg. Comparisons are presented in the streamwise and circumferential directions. The calculated results were obtained using grids with differing amounts of circumferential resolution. Three grids were constructed, the first with 33 equally spaced circumferential points, the second with 65, and the third with 97. All grids had 65 streamwise points and 81 points between the body and outer boundary. Grid points were clustered near the body so that the cell Reynolds number was approximately one, and three grid levels were used in the multigrid procedure.

In Fig. 2, the predicted heating rate nondimensionalized by a theoretical stagnation heating-rate value is plotted against axial length nondimensionalized by the cone nose radius. Three LAURA predictions are plotted; one shown by a solid line that denotes the 33-point solution, another shown by a dashed line that denotes the 65-point solution, and the third shown by a dot-dashed line that denotes the 97-point solution. The circumferential angle ϕ equal to 0 and 180 deg corresponds to the upper and lower symmetry planes, respectively, and $\phi = 90$ deg represents the side plane. No significant differences in heating are noted between the three predictions for $\phi = 180$ and 90 deg, and their agreement with the experimental data is within 10%. However, for $\phi = 0$ deg, the three predictions begin to differ at X/RN equal to 5.0, and their agreement deteriorates further downstream.

At ϕ approximately equal to 45 deg a crossflow shock develops, causing circumferential separation. This behavior is typical of many entry vehicles at angle of attack. Figure 3, a plot of upper-surface streamlines for the 33- and 65-point solutions, reveals the line of separation. Cleary believed the flow remained attached and that the rise

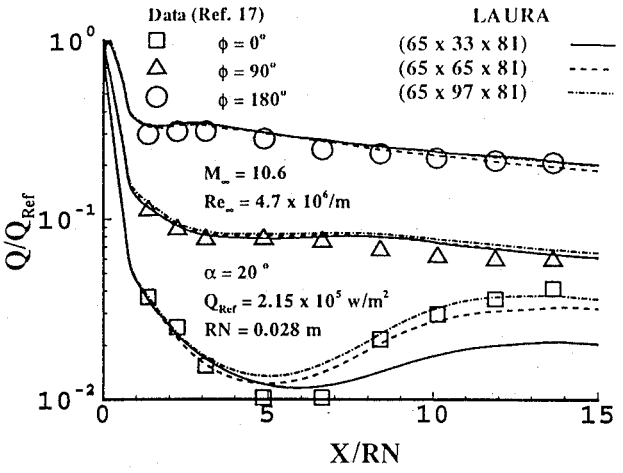

Fig. 2 Streamwise heating distributions on a 15-deg sphere-cone.

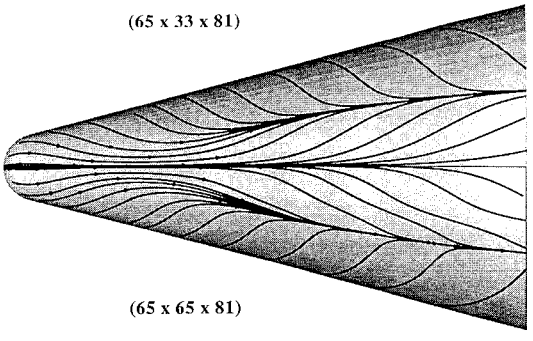

Fig. 3 Upper-surface streamlines.

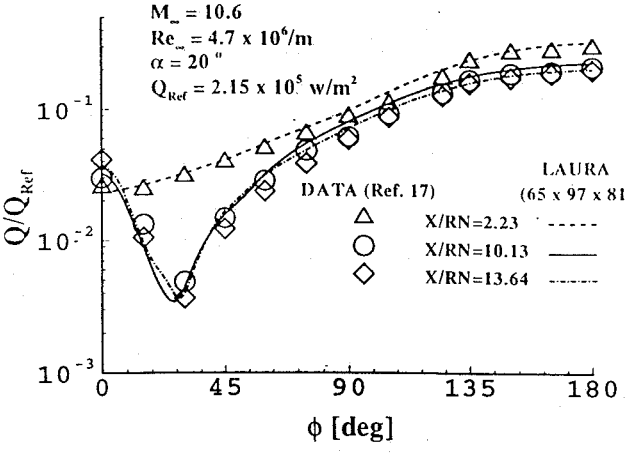

Fig. 4 Circumferential heating distributions on a 15-deg sphere-cone.

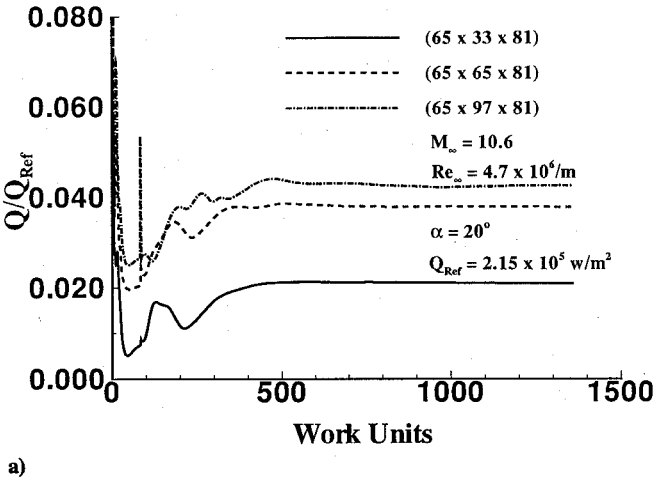

a)

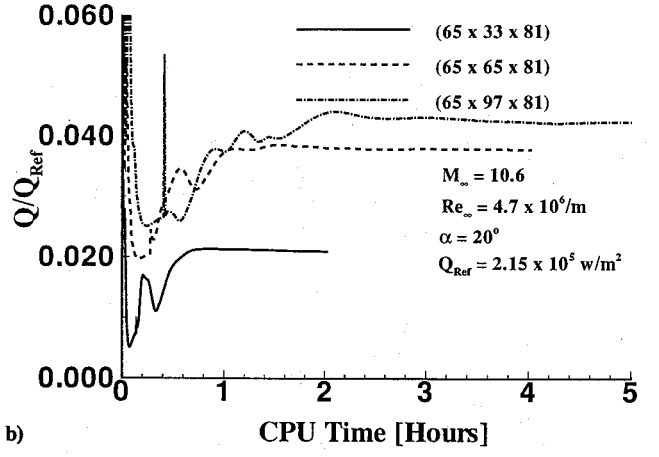

b)

Fig. 5 Surface heating-rate on a 15-deg sphere-cone: a) vs work units and b) vs CPU time.

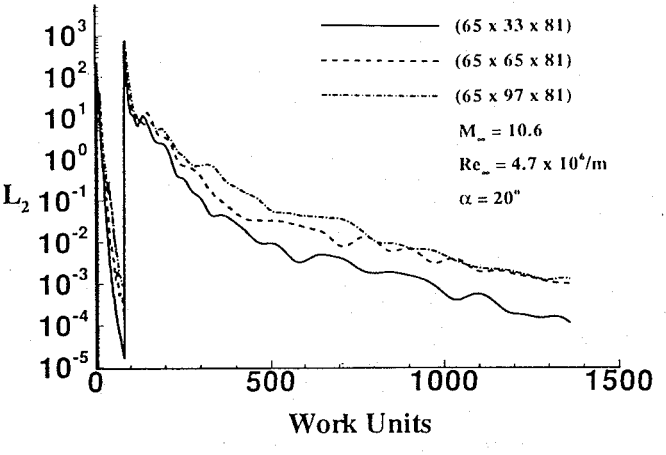

Fig. 6 Convergence history on a 15-deg sphere-cone.

in heating noted along the upper symmetry plane was due to transition. However, in subsequent work by Miller et al.[23] for biconics, laminar flow predictions from a parabolized Navier-Stokes (PNS) solver also show an increase in leeside heating, and the suggestion is that the rise is due to vortex reattachment. The circumferential grid resolution within the separated region has a strong influence on the upper-surface heating (Fig. 2). Increasing the resolution in this vortex region results in better agreement with the experimental data. With 65 circumferential points, LAURA is still underpredicting the heating on the far aft (X/RN =14) portion by 25% when compared with the experimental data. Agreement within 10% between prediction and experiment is obtained with 97 circumferential points. It is possible that by clustering points in the vortex region fewer than 97 may be required.

Circumferential surface heating-rate predictions at three axial stations (constant X/RN values) are presented in Fig. 4. In general, the 97-point LAURA solution for surface heating is in good agreement with experiment and indicates the same trends found in the experimental data. The highest heating values are found on the windward symmetry plane. Proceeding to the leeward surface, the values decrease to a minimum, and then rise in the area of vortex reattachment. The minimum in heating occurs within the region of separated flow, with its location approximately 13 deg after the point of circumferential separation. For X/RN equal to 2.23 and 10.13, agreement within ±10% is achieved from the lower symmetry plane (ϕ = 180 deg), around to the side plane (ϕ = 90 deg) through the separated region(ϕ < 45 deg) to the upper symmetry plane (ϕ = 0 deg). For X/RN equal to 13.64, agreement within ±10% is noted until the side plane (ϕ = 90). Between the side plane and the minimum in heat-

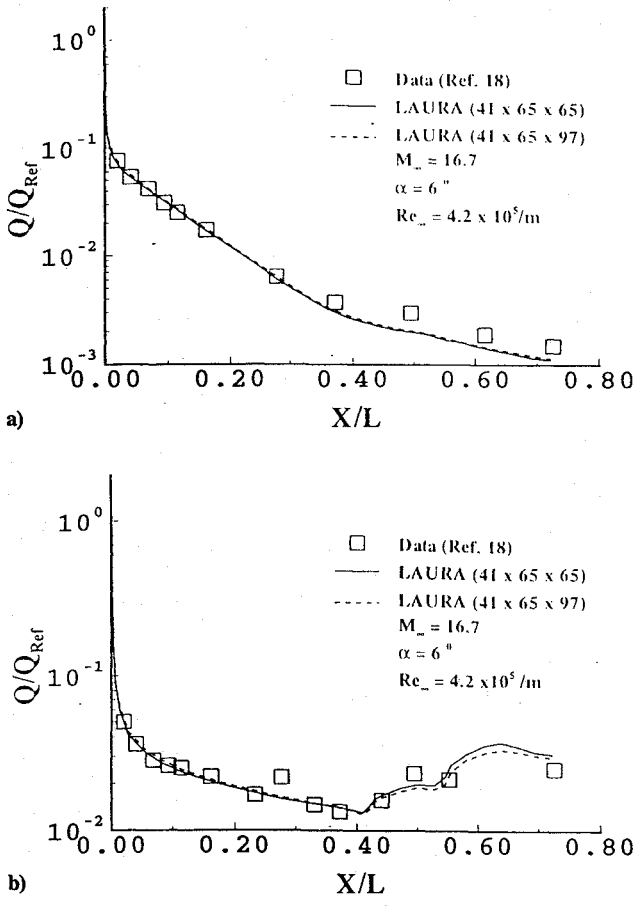

Fig. 7 Heating distribution on the blended wing-body: a) upper-symmetry-plane and b) lower-symmetry-plane.

ing, LAURA overpredicts the experimental data. The reason for this larger discrepancy is not known. Past the minimum the agreement improves to ±10%.

As a measure of convergence, some quantity integrated over the surface is usually examined. For inviscid flows, pressure in the form of the lift coefficient is typically monitored. Because gradient quantities in the boundary layer evolve much slower than the pressure field, the surface heating or skin friction is a more appropriate choice for viscous flows. In some instances, values at different locations within a domain can vary by orders of magnitude. Because integrated quantities are made up of values taken over the entire domain, large changes in relatively small values are not reflected. This could lead to a solution appearing to be converged when, in reality, small values are still undergoing large changes. To avoid this problem, the surface heating at a point where it is slow to converge is monitored over time. Figure 5a shows the surface heating at the extreme aft leeward symmetry plane plotted against work units for the three grids mentioned. One work unit is equivalent to one iteration on the finest mesh. Note from the figure, convergence was obtained in approximately 500 work units regardless of the number of grid points. In terms of CPU time, Fig. 5b shows negligible changes in the heating after 0.8 h for the 33-point solution, 1.7 h for the 65-point solution, and 2.5 h for the 97-point solution. This convergence behavior, the independence of work units and grid size for a given problem, and the linear relation between the CPU time and grid size are expected for a multigrid solver. Based on computational rates stated in Ref. 20, the nonmultigrid algorithm would require at least a factor of 3 more CPU time than the multigrid algorithm. The convergence history for the three solutions is presented in Fig. 6. The error in the right-hand-side residual when on the fine mesh is measured using a L_2 norm and is plotted against the number of work units.

Blended Wing-Body

This generic NASP configuration was used as part of a code calibration study. Heating rates predicted using LAURA were com-

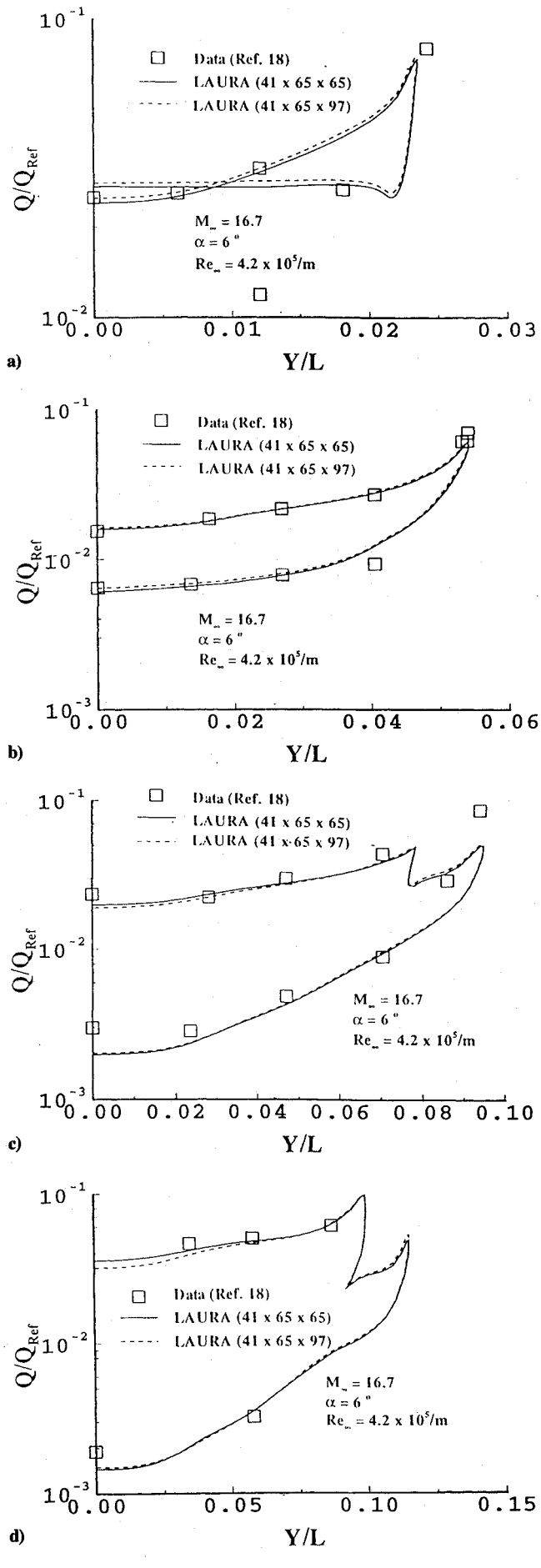

Fig. 8 Circumferential heating distribution on the blended wing-body at X/L =: a) 0.132, b) 0.294, c) 0.513, and d) 0.633.

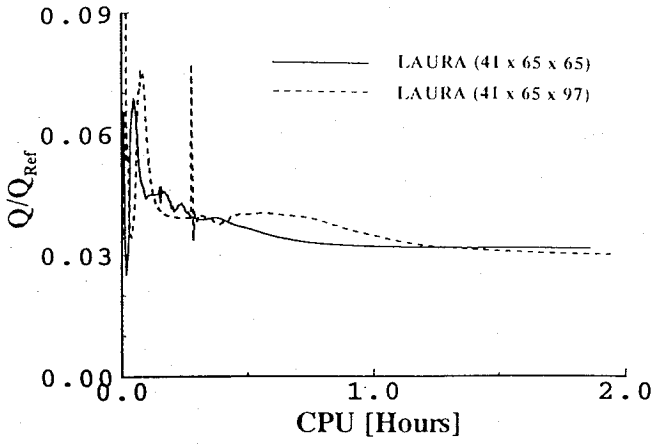

Fig. 9 Surface heating-rate history on the blended wing-body.

pared with the experimental data contained in Ref. 19. The flow was laminar with a freestream Mach number equal to 16.7, and the model was at 6-deg angle of attack. Presented are comparisons along the symmetry planes and around the vehicle's circumference at selected streamwise locations. To determine the effects of normal grid density, two solutions were computed, one with 65 points between the body and outer boundary, and a second with 97 points. Both computations used a surface grid that had 41 streamwise and 65 circumferential points. Surface grids with increased resolution were not available. The cell Reynolds number at the wall was approximately one. Three grid levels were used in the multigrid solution procedure.

Surface heating rates for the blended wing-body are plotted in Fig. 7. The 65-point solution is represented by the solid line, and the 97-point solution by the dashed line. Figures 7a and 7b are plots of nondimensional heating along the upper and the lower symmetry plane, respectively, versus nondimensional axial length. On the upper symmetry plane, no effects of normal grid density are noted. The differences between the computed predictions are negligible, and each solution compares well with the experimental data. Prior to $X/L = 0.4$, the results of LAURA are in agreement with the data, differing by a few percent. Aft of this location the difference grows, with the LAURA solutions underpredicting experiment by 30%. This may be caused by inadequate surface grid resolution, resulting in an inability to accurately predict the crossflow separation present in this region. Figure 7b is a plot of the windward surface heating. The two rises in heating ($X/L = 0.40$ and 0.55) are caused by the compression ramps. Differences due to changes in normal grid density are not significant until the second compression ramp, with the 97-point prediction a few percent lower. The LAURA solutions are within 5% of the experimental data, with the 97-point solution in slightly better agreement with the data along the second compression ramp ($X/L > 0.55$).

Figures 8a–8d present surface heating in the circumferential direction at four axial locations. The nondimensional heating is plotted against a nondimensional spanwise length. Typical of all circumferential distributions, upon moving away from the windward symmetry plane, the heating increases to a peak before the flow expands onto the leeward surface. Note that with the exception of the heating shown in Fig. 8a, the heating on the windward surface symmetry plane is higher than that found on the leeward symmetry plane. In Fig. 8a, the trend is reversed because of the low angle of attack and model geometry. At low angles of attack, the upper surface has a larger inclination to the flow than the lower surface. For a constant value of X/L, on the windward surface as the vehicle leading edge is approached, the lateral component of velocity increases and the boundary layer thins, causing the first peak in heating. In Figs. 8c–8d, after the first peak, a small reduction in heating occurs before a second rise is noted. The second rise is in the area between the compression ramp and leading edge. In general, the results are within $\pm 10\%$ of the experimental data, except when predicting the peaks aft of the vehicle, and where the leeside flow has separated.

Thompson and Gnoffo[17] computed the flow over the BWB with a $41 \times 65 \times 65$ grid using the single grid LAURA algorithm. This computation, which required 6.5 h on a Cray-2, translates into approximately 3.4 h on a CrayY-MP. Figure 9 is a plot of the nondimensional heating rate at the extreme aft windward symmetry plane against CPU time from the multigrid algorithm. The figure indicates 1 h is needed to converge the heating for the 65-point solution, and 1.5 h for the 97-point solution. This comparison represent a factor-3.4 decrease in CPU time for the multigrid algorithm with respect to the single-grid algorithm using the same grid dimensions. Also, note that the time required for a multigrid solution scales linearly with the number of grid points.

Concluding Remarks

A multigrid solution procedure has been incorporated in a version of the Langley aerothermodynamic upwind relaxation algorithm. This computational tool has been applied to several geometries in hypersonic flow at various angles of attack. While the LAURA code is not optimally suited for multigrid applications, the modified code can provide solutions in one-third the CPU time needed by the single-grid code. For hypersonic predictions over geometrically complex configurations that required tens of hours of CPU time, the computer time saving is significant. The predicted heat-transfer information compares well with experimental values. These values were predicted in the presence of separated flow, embedded shocks, and strong bow shocks.

References

[1]Yamamoto, Y., Akimoto, T., and Suzuki, N., "Numerical Simulation of Hypersonic Viscous Flow for the Design of H-II Orbiting Plane," AIAA Paper 90-0601, Jan. 1990.

[2]Greene, F. A., Weilmuenster, K. J., and Micol, J. R., "Predicted Aerodynamics for a Proposed Personnel Launch Vehicle," AIAA Paper 90-1668, June 1990.

[3]Kleb, W. L., and Weilmuenster, K. J., "Characteristics of the Shuttle Orbiter Leeside Flow During a Reentry Condition," AIAA Paper 92-2951, July 1992.

[4]Weilmuenster, K. J., and Greene, F. A., "A CFD Analysis of the HL-20/PLS," *Journal of Spacecraft and Rockets,* Vol. 30, No. 5, 1993, pp. 558–566.

[5]Weilmuenster, K. J., and Gnoffo P. A., "Solution Strategies and Heat Transfer Calculations for Three-Dimensional Configurations at Hypersonic Speeds,"*Journal of Spacecraft and Rockets,* Vol. 30, No. 4, 1993, pp. 385–394.

[6]Brandt, A., "Guide to Multigrid Development," *Lecture Notes in Mathematics,* Vol. 960, Springer-Verlag, Berlin, 1981, pp. 230–312.

[7]Jameson, A., and Baker, T. J., "Multigrid Solutions of the Euler Equations for Aircraft Configurations," AIAA Paper 84-0093, Jan. 1983.

[8]Jameson, A., and Yoon, S., "Lower-Upper Implicit Schemes with Multiple Grids for the Euler Equations," *AIAA Journal,* Vol. 25, No. 7, 1987, pp. 929-935.

[9]Radespiel, R., Rossow, C., and Swanson, R. C., "Efficient Cell-Vertex Multigrid Scheme for the Three-Dimensional Navier-Stokes Equations," AIAA Paper 89-1953, June 1989.

[10]Turkel, E., Swanson, R. C., Vatsa, V. N., and White, J. A., "Multigrid for Hypersonic Viscous Two- and Three-Dimensional Flows," NASA CR 187603, July 1991.

[11]Radespiel, R., and Swanson, R. C., "Progress with Multigrid Schemes for Hypersonic Flow Problems," NASA CR 189579, Dec. 1991.

[12]Vatsa, V. N., Turkel, E., and Abolhassani, J. S., "Extension of Multigrid Methodology to Supersonic/Hypersonic 3-D Viscous Flows," NASA CR 187612, Aug. 1991.

[13]Swanson, R. C, Turkel, E., and White, J. A., "An Effective Multigrid Method for High-Speed Flows," NASA CR 187602, July 1991.

[14]Vatsa, V. N., "Evaluation of a Multigrid-Based Navier-Stokes Solver for Aerothermodynamic Computations," AIAA Paper 92-4563, Aug. 1992.

[15]Gnoffo, P. A., "An Upwind-Biased Point-Implicit Relaxation Algorithm for Viscous, Compressible Perfect-Gas Flow," NASA TP 2953, Feb. 1990.

[16]Gnoffo, P. A., Gupta, R. N., and Shinn, J. L., "Conservation Equations and Physical Models for Hypersonic Air Flows in Thermal and Chemical Nonequilibrium," NASA TP 2867, Feb. 1989.

[17]Thompson, R. A., and Gnoffo, P. A., "Application of the LAURA Code for Slender-Vehicle Aerothermodynamics," *Journal of Spacecraft and Rockets,* Vol. 29, No. 1, 1992, pp. 16–23.
[18]Cleary, J. W., "Effects of Angle of Attack and Bluntness on Laminar Heating-Rate Distributions of a 15° Cone at a Mach Number of 10.6," NASA TN D-5450, Oct. 1969.
[19]Lau, K. Y., and Cosner, R. R., "Generic Technology Option # 2—Final Report; Volume IV—Blended Wing Body Aerothermal Model and Test Program," McDonnell Douglas Corp., July 1988.
[20]Greene, F. A., and Gupta, R. N., "Viscous Equilibrium Computations Using Program LAURA," *Journal of Spacecraft and Rockets,* Vol. 29, No. 5, 1992, pp. 627–632.
[21]Roe, P. L., "Approximate Riemann Solvers, Parameter Vectors and Difference Schemes," *Journal of Computational Physics,* Vol. 43, No. 2, 1981, pp. 357–372.
[22]Yee, H. C., "On Symmetric and Upwind TVD Schemes," NASA TM 86842, Sept. 1985.
[23]Miller, C. G., Wilder, S. E., and Gnoffo, P. A., "Measured and Predicted Vortex-Induced Leeward Heating on a Biconic at Mach 6 and 10," AIAA Paper 85-1061, June 1985.